

Multipath Interference Suppression of Amplitude-Modulated Continuous Wave Scanning LiDAR Based on Bayesian-Optimized XGBoost Ensemble

Sunghyun Lee, Yoonseop Lim, Wookhyeon Kwon, Yonghwa Park, *Member, IEEE*

Abstract—This paper proposes a novel multipath interference (MPI) suppression algorithm based on Bayesian-optimized extreme gradient boosting (XGBoost) ensemble to reduce MPI error in amplitude-modulated continuous wave (AMCW) scanning light detection and ranging (LiDAR). Contrast to this paper, many previous research works have focused on the MPI suppression in conventional AMCW time-of-flight (ToF) sensors with flash type illumination sources. However, the mitigated MPI error of these previous works still remains cm-scale due to the inherent limitation of illumination source and lack of MPI data. Meanwhile, since there exist few previous works for coaxial type AMCW scanning LiDAR, the MPI in such LiDAR still has not been validated. To achieve mm-scale MPI error mitigation regarding aforementioned issues, this paper proposes a MPI error correction algorithm based on Bayesian-optimized XGBoost ensemble and its implementation in coaxial type AMCW scanning LiDAR. To train the XGBoost ensemble, the MPI synthetic dataset generated by customized simulation is used in this paper. According to validation results, the mean absolute error (MAE) of MPI error originally 9.8 mm can be reduced to less than 2 mm by Bayesian-optimized XGBoost in simulation dataset. Such precise MPI mitigation results are also maintained in real object scenes. Specifically, the MAE of MPI error in measurement condition similar with public dataset is reduced to 2.8 mm, which is extremely low compared to other previous works.

Index Terms—Amplitude-modulated continuous wave (AMCW), light detection and ranging (LiDAR), multipath interference (MPI), simulation model, extreme gradient boosting (XGBoost), Bayesian optimization.

I. INTRODUCTION

DEPTH information is widely used nowadays for the precise object recognition of intelligent mechatronic systems. In field robotics, autonomous robots and vehicles generally utilize 3D coordinate information extracted from depth map for their localization, indoor mapping, and obstacle detection [1], [2]. Such 3D depth information is also utilized to provide human pose information for many engineering applications [3]. Likewise, the utilization of 3D depth information is already a main trend for the visual recognition of state-of-the-art intelligent systems and devices.

Amplitude-modulated continuous wave (AMCW) laser rangefinder is one of typical 3D depth measurement methods

[4], [5]. The main principle of the AMCW ToF sensor is to measure the phase delay of modulated laser signal reflected from object using demodulation pixel [6]–[8]. Since such AMCW time-of-flight (ToF) sensor shows precise distance measurement performance in relatively short range, many researchers have used various kinds of AMCW ToF sensors. The majority of AMCW ToF sensors adopt flash type illumination optics with CMOS demodulation pixel arrays to capture wide field-of-view (FoV) scene.

However, due to the optical characteristics of conventional ToF sensors and limitation of AMCW principle, there exist some problems related to distance measurement error such as phase ambiguity [9], fixed pattern noise [4], [10], thermal fluctuation [4], [10], etc. These issues can be easily corrected by utilizing look-up table (LUT) and various spatial image processing methods, according to many previous research works [4], [10]. On the other hand, multipath interference (MPI), which is non-systematic error, is still a challenging research issue.

Among aforementioned research issues related to conventional AMCW ToF sensors, the MPI problem has been most dealt with by many researchers recently [11]–[22]. Since the illuminated light is spread over the entire object scene by diffuser, multiple rays of light from unwanted region can also enter unintended demodulation pixel. Unfortunately, due to the inherent optical characteristics of conventional AMCW ToF sensors, the existence of MPI is inevitable. Since it is not feasible to directly get rid of the MPI itself, many researchers had attempted to reduce the MPI error using post-error correction methods. One of MPI mitigation method is based on numerical optimization. Dorrington *et al.* [15] assumed two-path model for MPI, and designed L_2 norm objective function composed of measured and estimated correlations to solve true range using least-square approach. Kirmani *et al.* [16] also assumed multipath model as N discrete paths, and estimated multipath parameters using total least square (TLS) Prony's method. Meanwhile, Freedman *et al.* [11] used sparse reflections analysis (SRA) method to validate two-path MPI model with data measured in the condition of 3 different modulation frequencies. With similar concepts, Feigin *et al.* [12] used matrix pencil method which is one of spectral estimation methods to find out true range from the data measured with 3 modulation frequencies. All these aforementioned previous works assume MPI model as two or more number of light paths, and solve the true range based on convex optimization or spectral estimation. However, the

Sunghyun Lee, Yoonseop Lim, and Yonghwa Park are with the Department of Mechanical Engineering, Korea Advanced Institute of Science and Technology, Republic of Korea. (shleetop@kaist.ac.kr, bu2050@kaist.ac.kr, yhpark@kaist.ac.kr, *corresponding author*: Yonghwa Park)
Wookhyeon Kwon is with the Mechatronics Research, Samsung Electronics Co., Republic of Korea. (wookoo.kwon@samsung.com)

> REPLACE THIS LINE WITH YOUR MANUSCRIPT ID NUMBER (DOUBLE-CLICK HERE TO EDIT) <

optimization solver is relatively slow making real-time implementation hard. Moreover, although two-path MPI model is quite fit well with many conventional AMCW ToF sensors, there still exist lots of redundant rays of light in actual MPI situation.

To confront such imperfect light transport model and slow calculation process, many researchers have utilized post-correction models based on deep learning approach in these days. The majority of deep learning-based approaches generally adopt convolutional neural network (CNN) architectures [13], [14], [17]–[21]. Marco *et al.* [21] proposed convolutional autoencoder (CAE) architecture to train synthetic MPI data set. Agresti *et al.* [17] suggested coarse-to-fine CNN architecture to train synthetic MPI data set generated by generative adversarial networks (GAN) and small amount of real MPI dataset. Meanwhile, unlike other CNN-based research works, Su *et al.* [18] used correlation image for training the CNN architecture, not depth image. As mentioned above, many research works for MPI mitigation mainly use 3D depth and amplitude images with multiple modulation frequencies to train CNN-based deep learning architecture. Some research works use deep neural network (DNN) to train MPI data, but such cases are rare [22]. The aforementioned CNN-based approaches can reduce the MPI error to cm-scale in real time by training the geometrical pattern of measured scene including MPI. However, generating accurate synthetic data set is still a challenging issue since the amount of real MPI images is limited. Moreover, as CNN architecture entirely depends on the geometrical patterns, the MPI reduction performance is not robust against the orientation of measured scene even for the same object.

In this paper, regarding the above mentioned issues, a different approach to reduce MPI is proposed and validated in both hardware and software levels. To reduce the inherent MPI error in hardware level, coaxial type scanning optics is combined with AMCW scheme [8], [23], [24]. As the laser beam is collimated in extremely small area with high optical signal-to-noise ratio (SNR), the inherent MPI error is much less than that of conventional ToF sensor. To further reduce such MPI error in software level, a pixel-wise nonlinear mapping function which matches input depth and amplitude with scalar output of true range is designed based on Bayesian-optimized eXtreme Gradient Boosting (XGBoost) ensemble [25], [26]. Unlike image input training architecture of CNN-based previous works, pixel-wise learning approach is newly adopted to avoid the dependence on geometrical pattern of measured scene. Meanwhile, to solve the issue related to the generation of training data, an exact simulation model of the AMCW scanning LiDAR is also designed and utilized to generate enough synthetic MPI dataset. The exact synthetic MPI dataset with 4 different modulation frequencies are then trained by XGBoost ensemble with optimized hyperparameters [27], [28]. For the hyperparameter optimization, tree-structured Parzen estimator (TPE) in Bayesian scheme is used. With fast evaluation speed, the proposed XGBoost-based MPI mitigation algorithm can reduce the MPI error to mm-scale according to

the validation results in this paper. Some previous research works related to the AMCW scanning LiDAR had ignored such MPI effect [29], [30]. To our best knowledge, this paper is the first case study for the MPI error in coaxial type AMCW scanning LiDAR. We anticipate that the proposed pixel-wise learning approach with precise simulation data can be one of solutions to reduce the MPI error of various coaxial type scanning LiDAR, not just confined to AMCW scheme.

II. PROBLEM STATEMENT FOR MULTIPATH INTERFERENCE OF AMCW TOF SENSORS

The general principle of AMCW ToF measurement is to estimate the phase delay of reflected light signal using the reference signal which is same as demodulation signal. These signals can be expressed as follows [4], [6], [8]:

$$r(t) = R \cdot \left(1 + \alpha \cdot \cos \left(w \left(t - \frac{2d}{c} \right) \right) \right) \quad (1)$$

$$s(t) = m \cdot \cos(wt) \quad (2)$$

$$w = 2\pi f \quad (3)$$

where $r(t)$ is the reflected light signal, α is modulation contrast, R is the reflectivity of scene, d is the distance, c is the velocity of light, $s(t)$ is the demodulation signal, m is the amplitude of $s(t)$, f is the modulation frequency. To estimate the phase delay, the reflected light signal should be demodulated using at least three different number of phase-shifted demodulation signals. This process can be expressed mathematically using correlation function as follows:

$$\begin{aligned} C(\tau_n) &= \frac{1}{T_{\text{int}}} \int_0^{T_{\text{int}}} r(t) \cdot s(t + \tau_n) dt \\ &= \frac{1}{T_{\text{int}}} \int_0^{T_{\text{int}}} R \cdot \left(1 + \alpha \cdot \cos \left(w \left(t - \frac{2d}{c} \right) \right) \right) \\ &\quad \times m \cdot \cos(w(t + \tau_n)) dt \\ &= R \cdot \frac{\alpha \cdot m}{2} \cos(w\tau_n + \phi(w)) (n = 1, 2, \dots, N_{\text{tap}}) \end{aligned} \quad (4)$$

$$\phi(w) = \frac{2d \cdot w}{c} = \frac{4\pi \cdot d \cdot f}{c} \quad (5)$$

where $C(\tau_n)$ is the cross correlation, τ_n is the time shift of demodulation signal, N_{tap} is the tap number of which is 4 in general, T_{int} is the integration time. By sampling 4 points of cross correlation in general, the phase delay $\phi(w)$ is calculated [6]–[8]. Meanwhile, to simply express the cross correlation with only essential information, *i.e.*, the amplitude and phase delay of correlation, phasor expression is generally used as follow [11], [12]:

$$C(w) = R \cdot \frac{\alpha \cdot m}{2} e^{j\phi(w)} = \Gamma \cdot e^{j\phi(w)} \quad (6)$$

where Γ is the amplitude of cross correlation, $\phi(w)$ is the phase delay of cross correlation. In ideal case, per demodulation pixel, only directly reflected light signal from specific object point is matched.

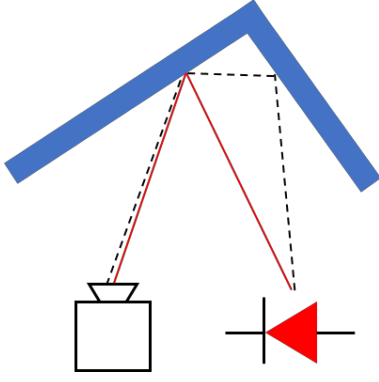


Fig. 1. Multipath interference in conventional AMCW ToF sensor. The red line is directly reflected light. The dotted black line is multi-reflected light.

However, as the illuminated light is spread over the entire object scene, other unwanted light signals also enter the unintended demodulation pixel as shown in Fig. 1. Consequently, the actual recorded cross correlation function in demodulation pixel is the summation of multiple complex vectors as follow [12], [20]:

$$C_{net}(w) = \Gamma_D \cdot e^{j\phi_D(w)} + \sum_{k=1}^{M-1} \Gamma_k \cdot e^{j\phi_k(w)} \quad (7)$$

where Γ_D , ϕ_D are amplitude and phase delay of directly reflected light, Γ_k , ϕ_k are amplitude and phase delay of k -th multi-reflected light, M is the total number of light paths. As shown in (7), the actual measured correlation inevitably includes multiple numbers of complex vectors of which modulation frequencies are all same. Due to the trigonometric property, the summation of all complex vectors in (7) resultantly is same as another single complex vector. Consequently, it is unreasonable to estimate ϕ_D using only single modulation frequency. To estimate ϕ_D correctly, measured data with multiple modulation frequencies is needed. The required number of modulation frequency is determined by the MPI model, *i.e.*, the number of light paths. Dorrington *et al.* [15] used two-path assumption ($M = 2$) for MPI. Since the intensity of MPI actually decays in exponential as the path length of MPI increases, it is quite reasonable to assume the MPI model using 2 paths of light [11], [16], [20]. Other previous research works also assume the number of MPI path as 2 or 3 in general [11]–[22]. Based on such assumed MPI models, many research works had improved the reduction of MPI error using various optimization methods and deep learning architectures.

However, there still exist some limitations in many previous works dealing with MPI. First, many researchers used less than 3 modulation frequencies although at least 4 modulation frequencies are required for two-path model. Such tendency is mainly due to the hardware limitation of conventional ToF sensors. Second, the actual complexity of MPI model in conventional AMCW ToF sensor is much higher than simple

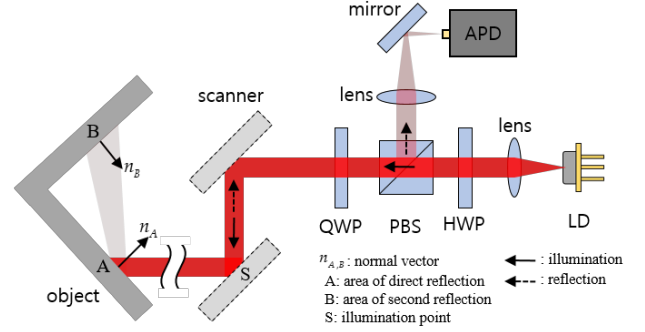


Fig. 2. Multipath interference in coaxial type AMCW scanning LiDAR. QWP is quarter-wave plate. PBS is polarizing beam splitter. HWP is half-wave plate. LD is laser diode. APD is avalanche photodiode.

two-path model. Namely, achieving precise model of the MPI in conventional ToF sensor is quite cumbersome due to the optical characteristics of flash type illumination source and pixel array resulting in low SNR of directly reflected light. At last, for the learning-based approaches, the lack of synthetic dataset also affects the MPI mitigation results in negative, causing over fitting. Consequently, due to the aforementioned limitations, the MPI mitigation results of many previous works still remain cm-scale.

To cope with aforementioned limitations, a pixel-wise learning approach based on Bayesian-optimized XGBoost is proposed and implemented in AMCW scanning LiDAR to reduce MPI error in this paper [8], [25], [26]. Additionally, to increase the information of directly reflected light, 4 different modulation frequencies are adopted. Meanwhile, to train the XGBoost-based pixel-wise MPI correction algorithm with enough and precise data, simulation model including the sensor noise characteristics of AMCW scanning LiDAR is proposed. Due the simplicity of coaxial optics and single avalanche photodiode (APD), modeling the simulation including MPI is much easier compared to conventional ToF sensors [8]. By training the XGBoost ensemble with precise MPI simulation data per pixel, the MPI error is reduced to mm-scale in various object scenes according to the validation results in this paper.

III. PIXEL-WISE MPI ERROR LEARNING APPROACH USING PRECISE SIMULATION DATA AND XGBOOST ENSEMBLE

A. Light Transport Model in AMCW Scanning LiDAR Simulation

The coaxial type scanning LiDAR has mainly two different aspects compared to the biaxial flash type ToF sensors. First, as the laser beam from scanning LiDAR is directly illuminated only on objective point of scene, the feasible MPI path is only confined to the case of triple reflection in the sequence of A, B, and A as shown in Fig. 2. Consequently, the optical SNR of directly reflected light to MPI in Fig. 2 is much higher than that of flash type conventional ToF sensor. Second, as the laser beam is collimated in very small area of which side length is

> REPLACE THIS LINE WITH YOUR MANUSCRIPT ID NUMBER (DOUBLE-CLICK HERE TO EDIT) <

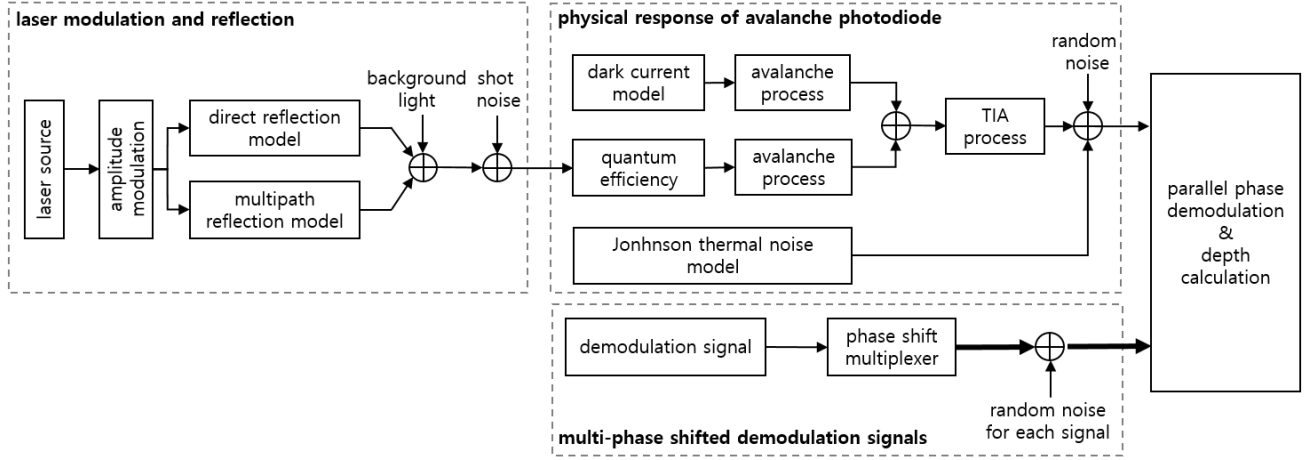


Fig. 3. Block diagram of simulation model for AMCW scanning LiDAR based on parallel-phase demodulation.

less than 5 mm, the MPI area close to the objective point is also relatively small and dense. Additionally, as the laser used in this paper is Gaussian beam, the intensity of MPI is also focused on center of MPI area. These aspects indicate that the lengths of all MPI light rays which round trip A and B in Fig. 2 are almost same. Considering aforementioned characteristics, it is reasonable to assume the MPI model in coaxial scanning LiDAR as two-paths shown in Fig. 2. Consequently, the total received light is the summation of directly reflected light from A and MPI light which round trip A and B, as shown in Fig. 2.

Based on the assumption of two-path model of light transport in coaxial scanning optics, the light transport equations are newly designed in this paper using the radiometric equations in many previous research works as follows [31], [32]:

$$R_d = I_s \cdot G_{S \rightarrow A}^S \cdot E_{AS} \quad (8)$$

$$R_{MPI} = I_s \cdot G_{S \rightarrow A}^B \cdot G_{A \rightarrow B}^A \cdot G_{B \rightarrow A}^S \cdot E_{AS} \quad (9)$$

$$E_{X \rightarrow Y} = \frac{S_Y \cdot \cos \theta_{YX}}{\|d_{XY}\|^2} \cdot e^{j\phi(d_{XY})} \quad (10)$$

$$G_{X \rightarrow Y}^Z = E_{X \rightarrow Y} \cdot \rho_{XYZ} \quad (11)$$

$$\cos(\theta_{XY}) = \frac{n_X \cdot \overline{XY}}{\|n_X\| \times \|XY\|} \quad (12)$$

$$R_{received} = R_d + R_{MPI} = I_s \cdot \left\{ G_{S \rightarrow A}^S + G_{S \rightarrow A}^B \cdot G_{A \rightarrow B}^A \cdot G_{B \rightarrow A}^S \right\} \cdot E_{AS} \quad (13)$$

where R_d , R_{MPI} are complex vector of directly reflected light and MPI in phasor, I_s is intensity of light source, E_{XY} is the intensity decrease and phase shift in complex vector due to light transport from X to Y , d_{XY} is the length between X and Y , $G_{X \rightarrow Y}^Z$ is the intensity decrease and phase shift in complex vector due to light transport from X to Y and reflection by surface Z , ρ_{XYZ} is the bidirectional reflectance distribution function (BRDF) of which the direction is X to Z through Y ,

n_X is the normal vector at surface X , S_X is the surface area of X , \overline{XY} is the position vector from X to Y . By controlling the model parameters in (13), numerous received light signals including MPI in simulation level can be generated and utilized to make precise synthetic MPI dataset reflecting the actual physics of light transport. Meanwhile, such light transport model in (13) is combined with sensor response model including electronic noise characteristics for precise AMCW scanning LiDAR simulation model in this paper.

B. Simulation model of AMCW Scanning LiDAR Based on Parallel-Phase Demodulation Including Noise Characteristics

The total received light signal including directly reflected light and MPI is generated following the light transport model in previous section. After this light signal is sensed by APD, various physical processes occur inside the electronic circuits of APD. Such sensor responses should be considered for the precise AMCW scanning LiDAR simulation model. To reflect such physical phenomena, all sensor noise characteristics are modeled in simulation as shown in Fig. 3.

In Fig. 3, after the laser source is modulated in sinusoidal as (1), the laser signal is reflected following the light transport model in (13). Then the incident number of received photons generated by reflected laser signal is expressed as follows [33]:

$$n_{ph} = \text{round} \left(\frac{P_{opt} \cdot t_{transit}}{E_p} \right) \quad (14)$$

$$E_p = \frac{hc}{\lambda} \quad (15)$$

where n_{ph} is the number of received photons, P_{opt} is the incident power of received light, $t_{transit}$ is the carrier transit time, E_p is the energy of photon, h is Planck constant, λ is wavelength of laser. However, the actual number of received photons is determined in stochastic due to the photon shot noise as follow [33]:

> REPLACE THIS LINE WITH YOUR MANUSCRIPT ID NUMBER (DOUBLE-CLICK HERE TO EDIT) <

$$n_{ph,shot} \sim P_{Poisson}(n_{ph,shot}; n_{ph}) = \frac{n_{ph}^{n_{ph,shot}} e^{-n_{ph}}}{n_{ph,shot}!} \quad (16)$$

where $n_{ph,shot}$ is the number of received photons with shot noise, $P_{Poisson}()$ is probability distribution function (PDF) following Poisson distribution. The received photons are then converted into electrons in APD and amplified by avalanche process as follows [33]:

$$n_{e^-} = n_{ph,shot} \cdot \eta + \varepsilon_{back} \quad (17)$$

$$\bar{n}_{ph,apd} = M \cdot n_{e^-} \quad (18)$$

$$\text{var}(n_{ph,apd}) = M^2 F \cdot n_{e^-} \quad (19)$$

$$n_{ph,apd} \sim N_{avalanche}(n_{ph,apd}; \bar{n}_{ph,apd}, \text{var}(n_{ph,apd})) \quad (20)$$

where n_{e^-} is the number of photoelectrons, η is quantum efficiency, ε_{back} is additional Gaussian noise due to background light, M is avalanche gain, F is excess noise factor, $n_{ph,apd}$ is amplified number of electrons after avalanche process, $\bar{n}_{ph,apd}$ is the average of $n_{ph,apd}$, $\text{var}(n_{ph,apd})$ is the variance of $n_{ph,apd}$, $N_{avalanche}()$ is the PDF of avalanche process which is same as Gaussian distribution. Such photoelectrons after avalanche process directly results in the photocurrent and corresponding voltage in APD as follows [34]–[36]:

$$I_{ph,apd} = \frac{n_{ph,apd} \cdot q}{t_{transit}} \quad (21)$$

$$V_{ph,apd} = I_{ph,apd} \cdot G \quad (22)$$

where q is the unit charge of electron, $I_{ph,apd}$ is the photocurrent generated by photoelectrons, $V_{ph,apd}$ is the corresponding voltage after amplification by transimpedance amplifier (TIA), G is the TIA gain.

Meanwhile, there exists another type of electric signal, *i.e.*, dark current. The dark current is the electric noise signal mainly affected by the physical characteristics and temperature of APD. The number of dark electrons with shot noise is expressed as follows [33], [37]:

$$n_{dark} = \text{round}\left(P_A I_{FM} T^{3/2} t_{transit} \exp\left(-\frac{E_g}{2k_B T}\right)\right) \quad (23)$$

$$n_{dark,shot} \sim P_{Poisson}(n_{dark,shot}; n_{dark}) \quad (24)$$

where n_{dark} is the number of dark electrons, P_A is the active area of APD, I_{FM} is dark current figure-of-merit, T is temperature, E_g is bandgap energy, k_B is Boltzmann constant, $n_{dark,shot}$ is the number of dark electrons with shot noise. The dark current in APD is then generated due to $n_{dark,shot}$ following (21).

Except for the dark current, TIA noise is generated during TIA process [34]. Additionally, thermal noise is also generated due to the load of circuits. Such TIA noise and thermal noise are not negligible for the precise sensor response model. All these physical processes are described as follows [34], [38], [39]:

$$n_{TIA} \sim N_{TIA}(n_{TIA}; \bar{n}_{TIA}, \text{var}(n_{TIA})) \quad (25)$$

$$\text{var}(n_{TIA}) = \frac{t_{transit}^2 S_{TIA} BW}{q^2} \quad (26)$$

$$I_{thermal} = \sqrt{\frac{4k_B T \cdot BW}{R_{Load}}} \quad (27)$$

where n_{TIA} is the number of TIA noise electrons, \bar{n}_{TIA} is the average of n_{TIA} , $\text{var}(n_{TIA})$ is the variance of n_{TIA} , $N_{TIA}()$ is the PDF of n_{TIA} same as Gaussian distribution, S_{TIA} is the spectrum intensity of TIA noise, BW is bandwidth, $I_{thermal}$ is the thermal noise current, R_{Load} is the load of circuit. In addition to thermal noise current in (27), the TIA noise current is also generated by n_{TIA} following (21).

After aforementioned processes, each current results in corresponding voltage following (22). Consequently, the total voltage response of APD due to light signals and all kinds of noises are as follows:

$$V_{apd} = V_{ph,apd} + V_{dark,apd} + V_{TIA} + V_{thermal} + \varepsilon_{rand} \quad (28)$$

where V_{apd} is the total voltage response of APD, V_x is the voltage generated by source x , ε_{rand} is additional random noise which is modeled as a simple Gaussian noise.

The output voltage in (28) is actually sinusoidal waveform as expressed in (1), which has no noise terms though. To demodulate (28), demodulation signal in (2) is generated in simulation as shown in Fig. 3. By multiplexing the demodulation signal with multiple phase shifts (generally 4 different phase shifts), the correlations are calculated in parallel in simulation environment. Using these cross correlations calculated by parallel-phase demodulation [8], the synthetic depth and amplitude of cross correlation are finally generated. By changing physical parameters of light transport model and APD response model, numerous synthetic MPI datasets can be generated to be used as training and validation dataset.

C. XGBoost Ensemble Optimized by TPE in Bayesian Scheme.

XGBoost was developed in 2016 by Chen *et al.* [25]. The basic principle of XGBoost is same as the gradient boosting method which learns residuals using multiple weak learners. Based on this ground, the XGBoost was improved in the aspects of overfitting, training speed, and precision. Compared to the conventional boosting methods, the XGBoost prevents overfitting using regularization term in loss function. Meanwhile, to speed up the training process, the XGBoost trains each classification and regression tree (CART) in parallel. Additionally, by adding second-order Taylor expansion to the loss function, the mathematical precision was improved. Except

> REPLACE THIS LINE WITH YOUR MANUSCRIPT ID NUMBER (DOUBLE-CLICK HERE TO EDIT) <

for these logical improvements, XGBoost utilizes prefetching considering cache for improved data interface which can decrease the training time dramatically. Due to such advantages of XGBoost, many researchers have adopted the XGBoost to solve various data-driven engineering problems recently [27], [40]. In this paper, the XGBoost is adopted as MPI data training regressor to precisely correct MPI error in AMCW scanning LiDAR. In the following paragraphs, the basic concepts and mathematical expressions of XGBoost are described.

The basic regression problem with K -CARTs are as follows:

$$\hat{y}_i = \sum_{t=1}^K f_t(x_i), f_t \in F \quad (29)$$

$$F = \left\{ f(x) = w_{q(x)} \mid w \in R^T \right\} \quad (30)$$

$$q: R^d \rightarrow \{1, 2, \dots, T\} \quad (31)$$

$$D = \{(x_i, y_i) \mid x \in R^d, y \in R\} (i = 1, 2, \dots, n) \quad (32)$$

where \hat{y} is estimated output by regressor, f is weak learner which belongs to the category F , F is the hypothesis space for all feasible CART learners, T is the number of leaf nodes in specific CART, w is the score vector of all leaf nodes, $q(x)$ is the mapping function which matches the input sample with leaf node of CART, D is the training dataset. To find optimal K -CARTs, the objective function is designed in XGBoost algorithm as follows:

$$J = \sum_{i=1}^n l(y_i, \hat{y}_i) + \sum_{t=1}^K \Omega(f_t) \quad (33)$$

$$\Omega(f_t) = \gamma T + \frac{1}{2} \lambda \sum_{j=1}^T w_j^2 \quad (34)$$

where J is the total objective function of XGBoost, l is the loss composed of target value and estimated value, Ω is the regularization term of CART, γ is the penalty coefficient related to the number of leaf node, λ is the penalty coefficient related to the square of weight. The training process of XGBoost is ultimately to minimize J . During training process, overfitting is prevented by the regularization term in (34). Meanwhile, during XGBoost training, the local objective function should be minimized for each new generation of CART in sequential. The local objective function is expressed as follow:

$$J^{(t)} = \sum_{i=1}^n l(y_i, \hat{y}_i^{t-1} + f_t(x_i)) + \Omega(f_t) \quad (35)$$

where $J^{(t)}$ is the objective function after t -th CART is generated, \hat{y}_i^{t-1} is the estimated value until $(t-1)$ -th CART. Using the second order Taylor expansion approximation, the loss function in (35) is much more simply expressed to be calculated in fast speed. All these processes are as follows:

$$J^{(t)} = \sum_{i=1}^n \left[l(y_i, \hat{y}_i^{t-1}) + g_i f_t(x_i) + \frac{1}{2} h_i f_t^2(x_i) \right] + \Omega(f_t) \quad (36)$$

$$g_i = \partial_{\hat{y}_i^{t-1}} l(y_i, \hat{y}_i^{t-1}) \quad (37)$$

$$h_i = \partial_{\hat{y}_i^{t-1}}^2 l(y_i, \hat{y}_i^{t-1}) \quad (38)$$

where g_i is the first order gradient statistics, h_i is the second order gradient statistics. By removing the constant terms in (36), the final objective function after t -th CART and corresponding optimal parameters are as follows:

$$\begin{aligned} J^{(t)} &= \sum_{i=1}^n \left[g_i f_t(x_i) + \frac{1}{2} h_i f_t^2(x_i) \right] + \gamma T + \frac{1}{2} \lambda \sum_{j=1}^T w_j^2 \\ &= \sum_{j=1}^T \left[\left(\sum_{i \in I_j} g_i \right) w_j + \frac{1}{2} \left(\sum_{i \in I_j} h_i + \lambda \right) w_j^2 \right] + \gamma T \end{aligned} \quad (39)$$

$$w_j^* = - \frac{\sum_{i \in I_j} g_i}{\sum_{i \in I_j} h_i + \lambda} \quad (40)$$

$$J^* = - \frac{1}{2} \sum_{j=1}^T \frac{\left(\sum_{i \in I_j} g_i \right)^2}{\sum_{i \in I_j} h_i + \lambda} + \gamma T \quad (41)$$

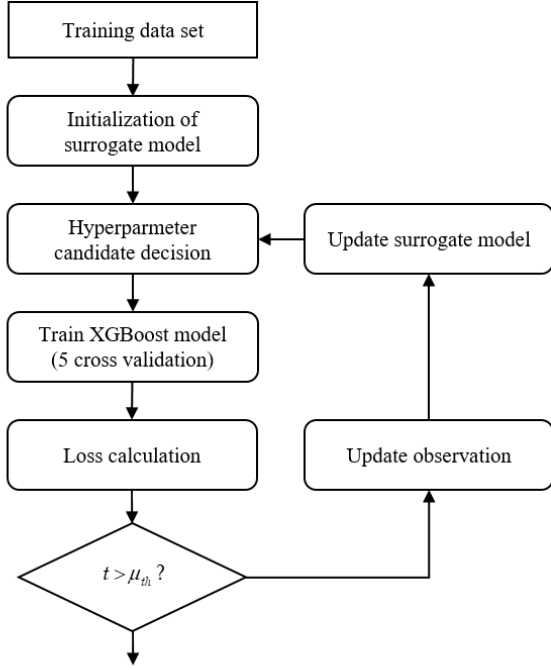
$$I_j = \{i \mid q(x_i) = j\} \quad (42)$$

where w_j^* is the optimal weight of leaf node j , J^* is the corresponding objective function of w^* . The training process of XGBoost is actually finding the optimal weight vector and related CART ensembles under the aforementioned processes using the given training dataset.

After optimal weight vector in (40) is fixed under the training process, the XGBoost regression in (29) is then used to estimate the correct distance taking the measured depth and amplitude with 4 different modulation frequencies as input vector. To train such XGBoost precisely, selection of proper hyperparameters is important. However, there exist many hyperparameters as shown above equations related to XGBoost, which makes manual tuning difficult. To select optimal hyperparameters of XGBoost model, TPE-based Bayesian optimization algorithm is adopted in this paper.

Basic backbone of many kinds of Bayesian optimization algorithms follows sequential model-based optimization (SMBO) [26]. In SMBO algorithm, a surrogate model to select optimal hyperparameter candidate is designed considering conditional PDF of observed hyperparameter set. By minimizing or maximizing the output of current surrogate, the optimal hyperparameter in current iteration is determined. After calculating the loss function using such hyperparameter, the loss and corresponding hyperparameter are updated in observed hyperparameter set. Based on this updated hyperparameter set, the surrogate model is also updated and next step is moved to the optimal hyperparameter decision again. All these processes are repeated until the iteration number overwhelms predetermined threshold. Such SMBO-based Bayesian scheme can be used for the hyperparameter optimization problems of various learning models due to its fast convergence speed and

> REPLACE THIS LINE WITH YOUR MANUSCRIPT ID NUMBER (DOUBLE-CLICK HERE TO EDIT) <



Optimized hyperparameters for XGBoost

Fig. 4. Flow chart of hyperparameter optimization based on TPE approach for XGBoost model.

robustness to model complexity [26]. Especially both the XGBoost model and Bayesian optimization process are capable of parallel and distributed computing, combination of these two processes has much synergy compared to other learning machines [27].

The overall flow chart of hyperparameter optimization in this paper is described in Fig. 4. The training dataset is generated by simulation model described in previous sections. Specifically, one training data pair includes 8 by 1 input vector composed of depth and amplitude with 4 different modulation frequencies, and its corresponding correct depth as target value. For the surrogate model in Fig. 4, the expectation improvement (EI) is adopted as the output of surrogate as follow:

$$EI(\xi) = \int_{-\infty}^{l^*} \max(l^* - l, 0) \cdot p_{S_t}(l | \xi) dl \quad (43)$$

where ξ is the hyperparameter, l is the corresponding loss, l^* is the threshold loss of current iteration, $p_{S_t}(l | \xi)$ is the conditional PDF of l to ξ in current surrogate of iteration t . The PDF in (43) is defined as follows:

$$p_{S_t}(l | \xi) = \begin{cases} h(\xi) & \text{if } l < l^* \\ g(\xi) & \text{if } l \geq l^* \end{cases} \quad (44)$$

$$p(l < l^*) = \beta \quad (45)$$

where $h(\xi)$ is the conditional PDF formed by observed ξ such that $l(\xi) < l^*$, $g(\xi)$ is the conditional PDF formed by remainder of observed hyperparameter set, β is the ratio between 0 and 1. In TPE-based optimization algorithm, h, g in (44) are modeled using Parzen estimator, which is one of non-

TABLE I
PARAMETERS FOR AMCW SCANNING LIDAR
SIMULATION

parameter	value	parameter	value
I_s	20 mW	η	0.67
α	1	M	50
f	12.5, 18.75, 25, 31.25 MHz	F	4.862
c	$3 \cdot 10^8$ m/s	q	$1.60217663 \cdot 10^{-19}$ C
d	1.4 ~ 2.4 m	p_A	0.7854 mm ²
m	0.4785 V	I_{EM}	1 nA/cm ²
θ_{XY}	$0 \sim \pi$ rad	T	297 K
ρ_{XYZ}	$0 \sim 1$	E_g	1.1116 eV
S_B	$0 \sim 7$ cm ²	k_B	$1.380649 \cdot 10^{-23}$ J/K
d_{AB}	$0 \sim 10$ cm	BW	50 MHz
$t_{transit}$	6 ns	S_{TIA}	$4.314 \cdot 10^{-24}$ A ² /Hz
λ	852 nm	R_{Load}	50 Ω
h	$6.62606896 \cdot 10^{-34}$ m ² kg/s	G	50 kV/A

parametric estimation models. As the distribution of variables are actually unknown, modeling the PDF with parametric model such as Gaussian process makes the optimization algorithm fall in local minima or diverge. To prevent such problems, Parzen estimators are adopted in this paper [26]. The new optimal hyperparameter is then determined as follow:

$$\xi^* = \arg \max_{\xi} \left\{ EI(\xi) \propto \left(\beta + \frac{g(\xi)}{h(\xi)} (1 - \beta) \right)^{-1} \right\} \quad (46)$$

where ξ^* is the optimal hyperparameter in current iteration. Using ξ^* , XGBoost is trained and used to calculate corresponding loss $l(\xi^*)$. If the current iteration t is lower than predetermined threshold μ_{th} , ξ^* and corresponding loss are added to the observation set to update surrogate model including (43) and (44). The optimization iteration is repeated until t exceeds μ_{th} . After the TPE-based hyperparameter optimization is finished, the final optimized hyperparameters of XGBoost are selected as Fig. 4. The XGBoost model with the optimized hyperparameters can estimate the correct depth taking the input vector including MPI error in mm-scale precision according to validation results in this paper. The detailed training process and validation results are described in the following section.

> REPLACE THIS LINE WITH YOUR MANUSCRIPT ID NUMBER (DOUBLE-CLICK HERE TO EDIT) <

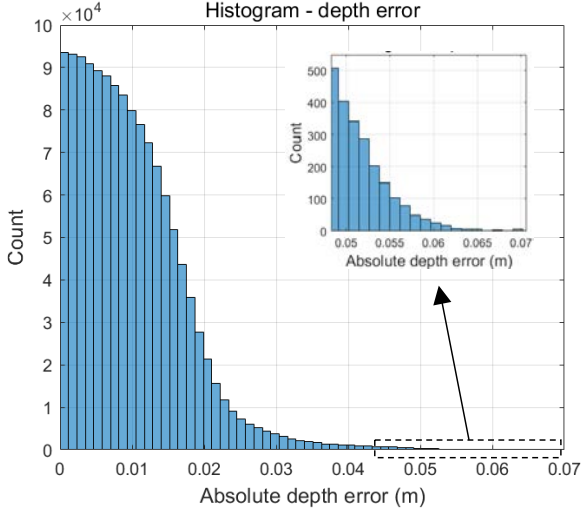


Fig. 5. Absolute depth error distribution due to MPI in simulation dataset.

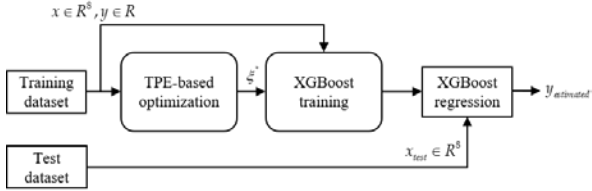


Fig. 6. Block diagram of correct depth estimation based on TPE-optimized XGBoost model.

IV. VALIDATION RESULTS OF MPI SUPPRESSION USING SIMULATION DATA AND OBJECT SCENES MEASURED BY AMCW SCANNING LiDAR

A. Validation of MPI suppression based on TPE-optimized XGBoost using MPI simulation data

To estimate correct depth using TPE-optimized XGBoost model, precise simulation training data is needed since acquisition of real MPI data is limited due to its amount and complexity of experimental conditions. To generate MPI simulation data which reflects the real measurement characteristics of AMCW scanning LiDAR, the model parameters in Table I were adopted for the simulation model in this paper. The range of parameters in Table I was widely determined for the comprehensive distribution of data. The total number of generated simulation dataset is 1,338,670. Each data includes 8 by 1 input vector which includes 4 pairs of depth and amplitude with different modulation frequencies, and corresponding scalar output as target depth. Meanwhile, the histogram of absolute depth error due to MPI in simulation dataset is plotted in Fig. 5. According to the Fig. 5, the mean absolute error (MAE) of MPI in simulation dataset is about 9.857 mm, which is extremely low compared to conventional ToF sensors. To further reduce such MPI error in AMCW scanning LiDAR, the hyperparameter optimization and training regressor should be conducted.

TABLE II
SUMMARY OF DEPTH ERROR CORRECTION PERFORMANCE INCLUDING MPI

	KNN	RF	SVM	DNN	XGBoost
RMSE-train (mm)	2.917	6.273	7.667	5.016	2.429
RMSE-test (mm)	3.645	6.344	7.692	4.577	2.760
MAE-train (mm)	1.926	4.675	5.597	3.535	1.759
MAE-test (mm)	2.467	4.727	5.621	3.548	1.960
Training time (sec)	1.272	54.93	95570	2838	267
Hardware	CPU	CPU	CPU	GPU	CPU

Before hyperparameter optimization and training process, the simulation data set is split into 2 parts: training dataset and test dataset. Specifically, 80% of simulation dataset is selected as training dataset, and the remainder as test dataset. With the selected training dataset, the TPE-optimized XGBoost is trained. The error correction performance is then validated using the test dataset. All these processes are shown in Fig. 6.

To evaluate the MPI suppression performance of TPE-optimized XGBoost more precisely, the comparison study with other widely used learning machines was conducted. Specifically, for the comparison, non-linear regression learning methods were adopted as follows: K-nearest neighbor (KNN) [41], random forest (RF) [42], support vector machine (SVM) [43], and deep neural network (DNN) with 2 hidden layers and LeakyReLU activation function [44]. For performance index, root mean square error (RMSE) and mean absolute error (MAE) between target depth and estimated depth were utilized. Meanwhile, to evaluate the model complexity, the training time was also compared for each learning-based regression model. The performance comparison for each regression model was conducted in both training dataset and test dataset. All the aforementioned validation results are shown in Table II. The hardware used for the training of KNN, RF, SVM, and XGBoost in Table II is Intel core i9-10900 with 16 GB RAM. Training of KNN, RF, and SVM were processed using python 3.8.8 with scikit-learn library version 1.0.2. For XGBoost training, python 3.8.8 with xgboost library version 1.6.0 was used. For the DNN training, the Quadro RTX 5000 manufactured by NVIDIA was used in same python environment. The library used for DNN training is PyTorch version 1.5.2. Including the XGBoost, other methods except for environment. The library used for DNN training is PyTorch version 1.5.2. Including the XGBoost, other methods except for

> REPLACE THIS LINE WITH YOUR MANUSCRIPT ID NUMBER (DOUBLE-CLICK HERE TO EDIT) <

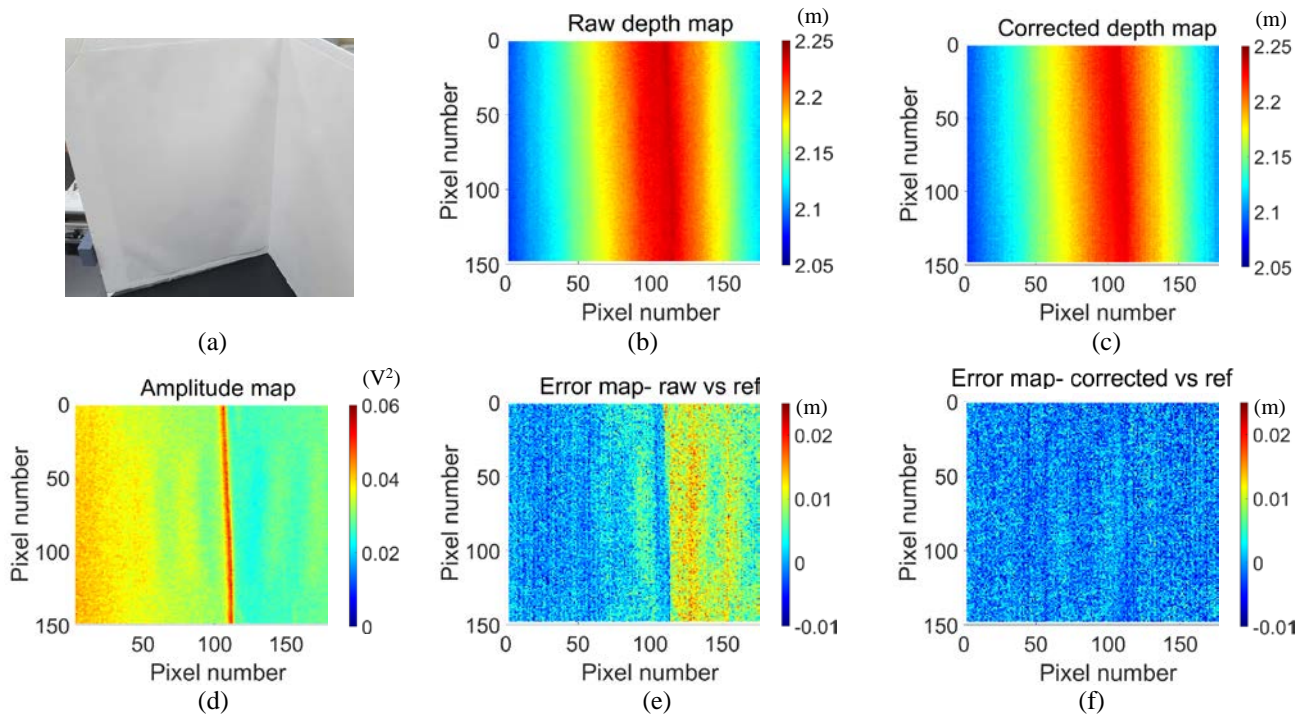


Fig. 7. Depth and amplitude map of cornered paper: (a) object, (b) raw depth map, (c) corrected depth map, (d) amplitude map (e) depth error map of raw data, (f) depth error map of corrected data.

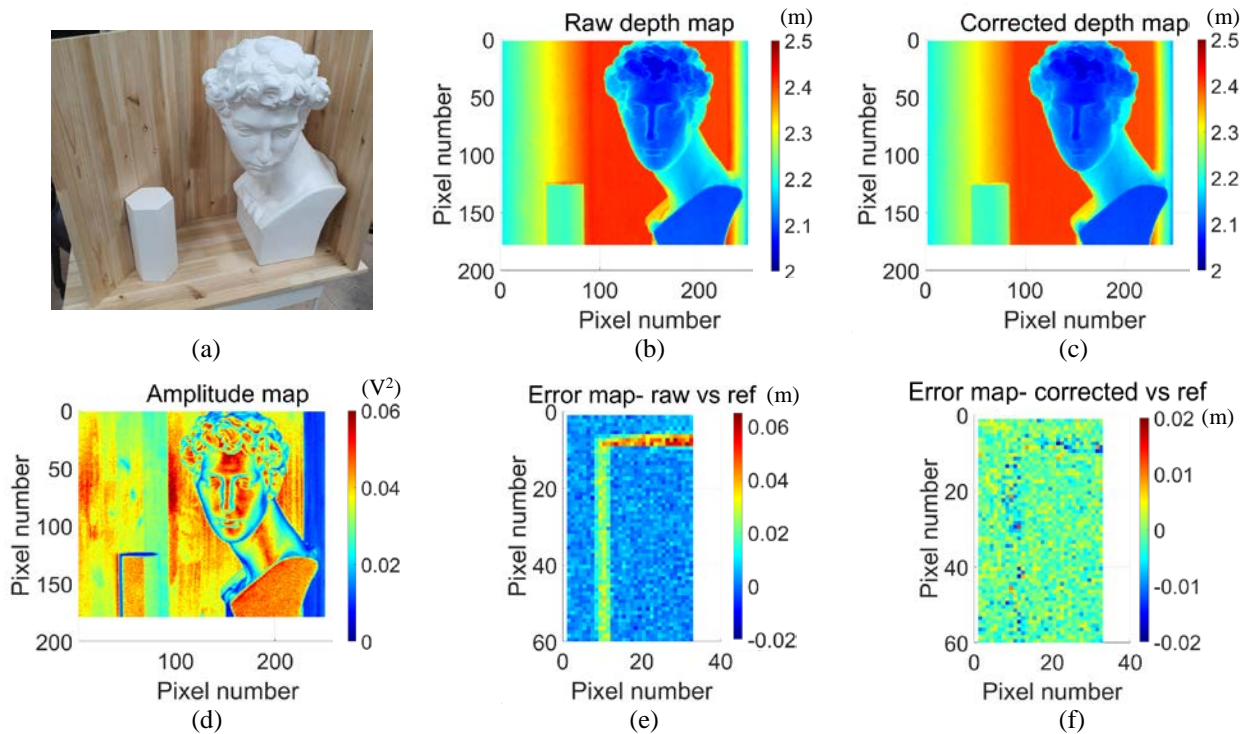


Fig. 8. Depth and amplitude map of multi-objects: (a) object, (b) raw depth map, (c) corrected depth map, (d) amplitude map (e) depth error map of raw data, (f) depth error map of corrected data.

SVM were also optimized by TPE-Bayesian scheme described in Fig. 4. The optimization tool used in this paper is Optuna [28].

According to Table II, the XGBoost shows the lowest RMSE and MAE in both training and test dataset compared to other learning regressions. Specifically in training dataset, the

> REPLACE THIS LINE WITH YOUR MANUSCRIPT ID NUMBER (DOUBLE-CLICK HERE TO EDIT) <

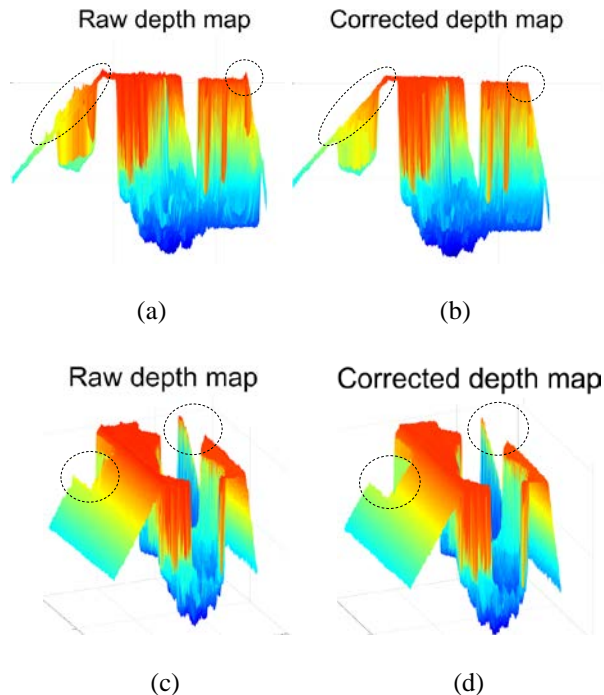


Fig. 9. Depth map of multi-objects: (a) raw data- top view, (b) corrected data- top view, (c) raw data- side view, (d) corrected data- side view.

RMSE and MAE of XGBoost are 2.429 mm and 1.759 mm, respectively. In test dataset, RMSE and MAE of XGBoost are 2.760 mm and 1.960 mm, respectively. Compared to the MAE in Fig. 5 originally 9.857 mm, about 80.12 % reduction of MAE was achieved by the XGBoost-based MPI correction in test dataset. Meanwhile, the RMSE difference between training dataset and test dataset is 0.331 mm, and MAE difference between training dataset and test dataset is 0.201 mm. These relatively small index variations indicate that the training process was conducted without overfitting.

The KNN method also shows low MAE in test dataset about 2.467 mm. This performance is better than that of RF, SVM, and even DNN, which is mainly attributed to the dense distribution of dataset. Especially, the training time of KNN is less than any regression methods due to its simplicity of model. However, the index variation between training and test dataset in MAE is over 0.5 mm which is much larger than that of XGBoost. This means that the KNN is relatively subject to the overfitting compared to other methods. The most inefficient method in Table II is SVM. The training time of SVM is over 24 hours which is extremely long compared to other methods. Such result is mainly due to the extremely many number of memorized support vectors. Moreover, the RMSE and MAE of SVM are larger than those of any other methods. Considering such problems related to time and performance, utilizing SVM is not reasonable for the MPI suppression problem in this paper. The remaining methods, RF and DNN, show moderate MAE and RMSE compared to those of SVM. Specifically, the MAE of RF and DNN in test dataset are 4.727 mm and 3.548 mm, respectively. One attracting point of RF is that the training time is under 60 seconds which is quite less than that of XGBoost.

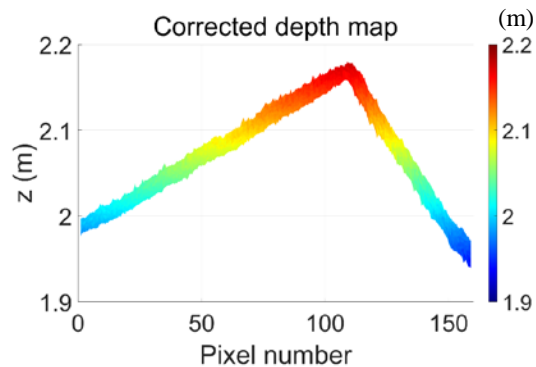


Fig. 10. Depth map of wooden structure- top view.

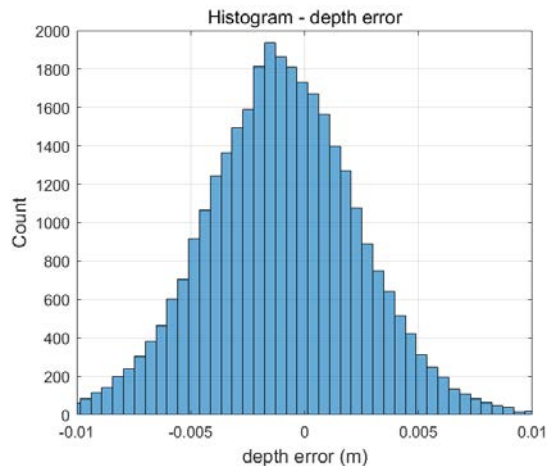


Fig. 11. Histogram of depth error in Fig. 10.

As all weak learners of RF are trained basically in parallel, the total training time can be less than that of XGBoost which depends on sequential-learner training structure. However, the difference of training time between RF and XGBoost is about 213 seconds which is tolerable in general. Such relatively tolerable training time difference is attributed to the parallel training process in each CART and distributing computing of XGBoost.

Regarding aforementioned characteristics of each learning regression method, it is easily deduced that utilizing the XGBoost is the most reasonable choice in terms of training time and performance. The XGBoost ensemble trained using simulation dataset and TPE-optimized hyperparameters was also validated in real 3D object scenes measured by AMCW scanning LiDAR.

B. MPI suppression of real 3D depth map measured by AMCW scanning LiDAR

To validate the MPI suppression performance of the proposed XGBoost-based regression model in Fig. 4 and 6, actual object scene including 4 depth maps and 4 amplitude maps were measured by AMCW scanning LiDAR based on parallel-phase demodulation. To acquire obvious MPI error data, multiple corners and sharp points were selected as object scenes. The physical quantities of LiDAR are as follows: 12.5, 18.75, 25, 31.25 MHz for multiple modulation frequencies, 20

> REPLACE THIS LINE WITH YOUR MANUSCRIPT ID NUMBER (DOUBLE-CLICK HERE TO EDIT) <

mW for laser power, 16 μsec for the integration time. For measurement environment, the wooden structure was constructed following the experimental setup of Agresti *et al.* [17] and Buratto *et al.* [20] for the comparison with other previous works. The measurement and MPI correction results are shown in Fig. 7 and Fig. 8. The cornered white paper in Fig. 7(a) was captured at the distance from 2.05 m to 2.25 m as shown in Fig. 7(b) and (c). To acquire depth error map, the reference map acquired by the geometric information was subtracted by the measured depth map as shown in Fig. 7(e) and (f). According to Fig. 7(e) and (f), the depth error due to MPI is mainly distributed near the boundary corner of white paper. Specifically, the distribution of depth error due to MPI in Fig. 7(e) is focused in the horizontal pixel region from 90 to 125, which is close the sharp corner of boundary. The maximum absolute depth error is about 2.4 cm in Fig. 7(e). Additionally, the right region of corner much suffers from the MPI error compared to the left region. Such tendency is due to the relatively low intensity of directly reflected light as shown in Fig. 7(d). However, the intensity of MPI error decreases as the pixel region is far from the corner in Fig. 7(e). Such MPI error is much mitigated by TPE-optimized XGBoost as shown in Fig. 7(f), although the noise-like patterns due to shot noise still exist. Specifically, the MAE of Fig. 7(e) which is 5.0 mm is reduced to 2.6 mm in Fig. 7(f).

To analyze MPI error distribution in more complex scene, multi-objects collocated in wooden structure were measured by AMCW scanning LiDAR as shown in Fig. 8. In Fig. 8(b), abrupt depth variation due to MPI exists near the boundary of wooden corners, left-bottom clavicle of Julien bust, and side corner between hexagonal pillar and wood. Compared to the raw depth map, the corrected depth map in Fig. 8(c) shows much more continuous depth variation in the aforementioned regions. For the quantitative comparison, the depth error maps were also acquired using both raw and corrected depth maps. However, as the Julien bust is geometrically complex, the reference map was generated only in geometrically simple region, as shown in Fig. 8(e) and (f). The maximum absolute depth error and the MAE in Fig. 8(e) are about 6.4 cm and 8.5 mm, respectively. Compared to the Fig. 7(e), the MAE of Fig. 8(e) is much larger due to much lower intensity of directly reflected light as shown in Fig. 8(d). Such low intensity of directly reflected light can be affected by many causes such as the reflectivity of material, relative position of object and sensor, exposure area of surface, the orientation of surface, etc. Namely, it can be deduced that the maximum absolute depth error and MAE in Fig. 8(e) are larger than those in Fig. 7(e) due to the aforementioned causes which are not quantitatively presentable though. In Fig. 8(f), the maximum absolute error and MAE are 2.1 cm and 3 mm, respectively. Although there still exist some errors around the corner of object scene, the majority of depth error was significantly suppressed as shown in Fig. 8(f). Such precise MPI suppression can be also identified in Fig. 9. As shown in Fig. 9, the entire scenes were captured in each top and side view using both raw and corrected depth maps to present the geometrical distortions caused by MPI. The geometrical distortions due to MPI marked by black dotted circle in Fig. 9(a) and (c) were effectively mitigated retaining the actual corner geometry as shown in Fig. 9(b) and (d).

Meanwhile, the comparison of the proposed MPI correction method with other previous works is required for the objective evaluation of the proposed method. Unfortunately, due to the different optical structure and modulation frequencies, the public dataset is not compatible with the proposed system and methods in this paper. Alternatively, to compare measurement precision of the proposed method with other previous works, the experimental condition was maintained similar with that of other previous works. Specifically, the wooden structure same as that of Agresti *et al.* [17] and Buratto *et al.* [20] was used for the comparison. As shown in Fig. 10, the corner is almost 90 degree and each wood plate is shown as flat. Specifically, the MAE in Fig. 10 is about 2.8 mm, which is extremely low compared to other previous works [17], [20]. Additionally, the distribution of depth error is described in Fig. 11. The depth error in Fig. 11 is not absolute value unlike other figures in previous sections, which can show the average bias of measured depth error. According to Fig. 11, the average bias of depth error is about 1 mm which is negligible. This means that the corrected depth map almost perfectly retains the geometrical information of measured scene even at much longer distance compared to other previous works.

V. CONCLUSION

In this paper, the pixel-wise learning approach based on TPE-optimized XGBoost algorithm was used to correct depth error caused by MPI in AMCW scanning LiDAR. To optimize the hyperparameter and train the XGBoost, simulation data in Table I was generated and utilized as training and test dataset as shown in Table II. According to Table II, the MAE after MPI correction was about 1.960 mm in test dataset. Such extremely low MAE of depth map was also maintained in real measured object scenes as shown in Fig. 7-11. Specifically, the MAE after correction of depth map was lower than 3 mm in various object scenes. To compare the proposed method with other previous works, a similar object was measured and analyzed in Fig. 10 and 11. Consequently, the MAE of the corrected depth map was about 2.8 mm, which is extremely low compared to other previous works. Such highly precise MPI correction performance of pixel-wise XGBoost regression is mainly attributed to two main characteristics as follows:

- 1) The inherently low MPI error due to optical characteristics of coaxial scanning LiDAR.
- 2) Precise training data with four modulation frequencies generated by customized simulation of AMCW scanning LiDAR.

For the future works, data generation scheme will be additionally improved to further reduce the MPI error in Fig. 8(f). Specifically, domain adaptation will be added to increase the precise training data [17]. Meanwhile, the hyperparameter optimization algorithm can be also modified using other kinds of architectures such as genetic algorithm [45]. Based on these improvements of MPI suppression algorithm, it is anticipated that this work will be utilized in various kinds of scanning LiDAR for the enhancement of 3D depth image quality.

References

- [1] H. Gao, B. Cheng, J. Wang, K. Li, J. Zhao, and D. Li, "Object Classification Using CNN-Based Fusion of Vision and LIDAR in Autonomous Vehicle Environment," *IEEE Trans. Ind. Informatics*, vol. 14, no. 9, pp. 4224–4230, 2018, doi: 10.1109/TII.2018.2822828.
- [2] F. Endres, J. Hess, N. Engelhard, J. Sturm, D. Cremers, and W. Burgard, "An evaluation of the RGB-D SLAM system," *Proc. - IEEE Int. Conf. Robot. Autom.*, vol. 1, no. c, pp. 1691–1696, 2012, doi: 10.1109/ICRA.2012.6225199.
- [3] S. Pasinetti, M. Muneeb Hassan, J. Eberhardt, M. Lancini, F. Docchio, and G. Sansoni, "Performance Analysis of the PMD Camboard Picoflexx Time-of-Flight Camera for Markerless Motion Capture Applications," *IEEE Trans. Instrum. Meas.*, vol. 68, no. 11, pp. 4456–4471, 2019, doi: 10.1109/TIM.2018.2889233.
- [4] S. Foix, G. Alenyà, and C. Torras, "Lock-in time-of-flight (ToF) cameras: A survey," *IEEE Sens. J.*, vol. 11, no. 9, pp. 1917–1926, 2011, doi: 10.1109/JSEN.2010.2101060.
- [5] Z. Wang, "Review of real-time three-dimensional shape measurement techniques," *Meas. J. Int. Meas. Confed.*, vol. 156, p. 107624, 2020, doi: 10.1016/j.measurement.2020.107624.
- [6] R. Lange and P. Seitz, "Solid-state time-of-flight range camera," *IEEE J. Quantum Electron.*, vol. 37, no. 3, pp. 390–397, 2001, doi: 10.1109/3.910448.
- [7] Y.-H. Park et al., "Three-dimensional imaging using fast micromachined electro-absorptive shutter," *J. Micro/Nanolithography, MEMS, MOEMS*, vol. 12, no. 2, p. 023011, 2013, doi: 10.1117/1.jmm.12.2.023011.
- [8] S. H. Lee, W. H. Kwon, Y. S. Lim, and Y. H. Park, "Highly precise AMCW time-of-flight scanning sensor based on parallel-phase demodulation," *Meas. J. Int. Meas. Confed.*, vol. 203, no. August, p. 111860, 2022, doi: 10.1016/j.measurement.2022.111860.
- [9] J. Wang, P. Liu, F. Wen, R. Ying, and W. Wang, "Phase Unwrapping for Time-of-Flight Sensor Based on Image Segmentation," *IEEE Sens. J.*, vol. 21, no. 19, pp. 21600–21611, 2021, doi: 10.1109/JSEN.2021.3101498.
- [10] Y. He and S. Chen, "Recent Advances in 3D Data Acquisition and Processing by Time-of-Flight Camera," *IEEE Access*, vol. 7, pp. 12495–12510, 2019, doi: 10.1109/ACCESS.2019.2891693.
- [11] D. Freedman, Y. Smolin, E. Krupka, I. Leichter, and M. Schmidt, "SRA: Fast removal of general multipath for ToF sensors," *Lect. Notes Comput. Sci. (including Subser. Lect. Notes Artif. Intell. Lect. Notes Bioinformatics)*, vol. 8689 LNCS, no. PART 1, pp. 234–249, 2014, doi: 10.1007/978-3-319-10590-1_16.
- [12] M. Feigin, A. Bhandari, S. Izadi, C. Rhemann, M. Schmidt, and R. Raskar, "Resolving Multipath Interference in Kinect: An Inverse Problem Approach," *IEEE Sens. J.*, vol. 16, no. 10, pp. 3419–3427, 2016, doi: 10.1109/JSEN.2015.2421360.
- [13] Q. Guo, I. Frosio, O. Gallo, T. Zickler, and J. Kautz, "Tackling 3D ToF Artifacts Through Learning and the FLAT Dataset," *Lect. Notes Comput. Sci. (including Subser. Lect. Notes Artif. Intell. Lect. Notes Bioinformatics)*, vol. 11205 LNCS, pp. 381–396, 2018, doi: 10.1007/978-3-030-01246-5_23.
- [14] G. Dong, Y. Zhang, and Z. Xiong, "Spatial Hierarchy Aware Residual Pyramid Network for Time-of-Flight Depth Denoising," *Lect. Notes Comput. Sci. (including Subser. Lect. Notes Artif. Intell. Lect. Notes Bioinformatics)*, vol. 12369 LNCS, pp. 35–50, 2020, doi: 10.1007/978-3-030-58586-0_3.
- [15] A. A. Dorrington, J. P. Godbaz, M. J. Cree, A. D. Payne, and L. V. Streeter, "Separating true range measurements from multi-path and scattering interference in commercial range cameras," *Three-Dimensional Imaging, Interact. Meas.*, vol. 7864, no. January 2011, p. 786404, 2011, doi: 10.1117/12.876586.
- [16] A. Kirmani, A. Benedetti, and P. A. Chou, "SPUMIC: Simultaneous phase unwrapping and multipath interference cancellation in time-of-flight cameras using spectral methods," *Proc. - IEEE Int. Conf. Multimed. Expo*, vol. 02139, no. 2, pp. 1–6, 2013, doi: 10.1109/ICME.2013.6607553.
- [17] G. Agresti et al., "Unsupervised domain adaptation for tof data denoising with adversarial learning" *IEEE CVPR*, pp. 5584–5593, 2019.
- [18] S. Su, F. Heide, G. Wetzstein, and W. Heidrich, "Deep End-to-End Time-of-Flight Imaging."
- [19] G. Agresti and P. Zanuttigh, "Deep learning for multi-path error removal in tof sensors," *Lect. Notes Comput. Sci. (including Subser. Lect. Notes Artif. Intell. Lect. Notes Bioinformatics)*, vol. 11131 LNCS, pp. 410–426, 2019, doi: 10.1007/978-3-030-11015-4_30.
- [20] E. Buratto, A. Simonetto, G. Agresti, H. Schäfer, and P. Zanuttigh, "Deep learning for transient image reconstruction from tof data," *Sensors*, vol. 21, no. 6, pp. 1–20, 2021, doi: 10.3390/s21061962.
- [21] J. Marco et al., "DeepToF: Off-the-shelf real-time correction of multipath interference in time-of-flight imaging," *ACM Trans. Graph.*, vol. 36, no. 6, 2017, doi: 10.1145/3130800.3130884.
- [22] K. Son, M. Y. Liu, and Y. Taguchi, "Learning to remove multipath distortions in Time-of-Flight range images for a robotic arm setup," *Proc. - IEEE Int. Conf. Robot. Autom.*, vol. 2016-June, pp. 3390–3397, 2016, doi: 10.1109/ICRA.2016.7487515.
- [23] S. H. Lee, W. H. Kwon, Y. Lim, and Y.-H. Park, "Distance measurement error compensation using machine learning for laser scanning AMCW time-of-flight sensor," vol. 1201303, no. March, p. 6, 2022, doi: 10.1117/12.2610458.
- [24] S. H. Lee, W.-H. Kwon, and Y.-H. Park, "Amplitude-modulated continuous wave scanning LIDAR based on parallel phase-demodulation," no. March, p. 15, 2021, doi: 10.1117/12.2577122.
- [25] C. Tianqi and G. Carlos, "Xgboost: A scalable tree boosting system," in *Proceedings of the 22nd acm sigkdd international conference on knowledge discovery and data mining. 2016, 2016*, p. 785.
- [26] J. Bergstra, R. Bardenet, Y. Bengio, and B. Kégl, "Algorithms for hyper-parameter optimization," *Adv. Neural Inf. Process. Syst. 24 25th Annu. Conf. Neural Inf. Process. Syst. 2011, NIPS 2011*, pp. 1–9, 2011.
- [27] Y. Xia, C. Liu, Y. Y. Li, and N. Liu, "A boosted decision tree approach using Bayesian hyper-parameter optimization for credit scoring," *Expert Syst. Appl.*, vol. 78, pp. 225–241, 2017, doi: 10.1016/j.eswa.2017.02.017.

> REPLACE THIS LINE WITH YOUR MANUSCRIPT ID NUMBER (DOUBLE-CLICK HERE TO EDIT) <

- [28] T. Akiba, S. Sano, T. Yanase, T. Ohta, and M. Koyama, "Optuna," pp. 2623–2631, 2019, doi: 10.1145/3292500.3330701.
- [29] Y. S. Jang, J. Park, and J. Jin, "Periodic-Error-Free All-Fiber Distance Measurement Method with Photonic Microwave Modulation Toward On-Chip-Based Devices," *IEEE Trans. Instrum. Meas.*, vol. 71, pp. 1–7, 2022, doi: 10.1109/TIM.2022.3146896.
- [30] S. Baek, "Centimeter-Wave Free-Space Neural Time-of-Flight Imaging," 2022.
- [31] D. Jiménez, D. Pizarro, M. Mazo, and S. Palazuelos, "Modeling and correction of multipath interference in time of flight cameras," *Image Vis. Comput.*, vol. 32, no. 1, pp. 1–13, 2014, doi: 10.1016/j.imavis.2013.10.008.
- [32] D. Bulczak, M. Lambers, and A. Kolb, "Quantified, interactive simulation of AMCW ToF camera including multipath effects," *Sensors (Switzerland)*, vol. 18, no. 1, 2018, doi: 10.3390/s18010013.
- [33] W. Huang and Z. Xu, "Characteristics and Performance of Image Sensor Communication," *IEEE Photonics J.*, vol. 9, no. 2, pp. 1–19, 2017, doi: 10.1109/JPHOT.2017.2681660.
- [34] A. S. Huntington, G. M. Williams, and A. O. Lee, "Modeling false alarm rate and related characteristics of laser ranging and LIDAR avalanche photodiode photoreceivers," *Opt. Eng.*, vol. 57, no. 07, p. 1, 2018, doi: 10.1117/1.oe.57.7.073106.
- [35] A. Huntington, "Sensitivity analysis of APD photoreceivers." VoxelOpto, Voxel Inc.: Beaverton, OR, USA, 2016, pp. 1-39.
- [36] Thorlabs, "APD120A(M) Operation Manual.", 2020.
- [37] M. Konnik and J. Welsh, "High-level numerical simulations of noise in CCD and CMOS photosensors: review and tutorial," pp. 1–21, 2014, [Online]. Available: <http://arxiv.org/abs/1412.4031>.
- [38] Hamamatsu Photonics, "Si APD, MPPC," in *Opto-semiconductor handbook*, 2014.
- [39] S. Kasap, "Optoelectronics and photonics : principles and practices", Second Edi. Pearson, 2013.
- [40] Y. Sha et al., "An acoustic signal cavitation detection framework based on XGBoost with adaptive selection feature engineering," *Meas. J. Int. Meas. Confed.*, vol. 192, no. February, p. 110897, 2022, doi: 10.1016/j.measurement.2022.110897.
- [41] Peterson, Leif E. "K-nearest neighbor." *Scholarpedia* 4.2 (2009): 1883.
- [42] M. Belgiu et al., "Random forest in remote sensing: A review of applications and future directions." *ISPRS journal of photogrammetry and remote sensing* 114 (2016): 24-31.
- [43] A. J. Smola et al., "A tutorial on support vector regression." *Statistics and computing* 14.3 (2004): 199-222.
- [44] Xu, Jin, et al. "Reluplex made more practical: Leaky ReLU." *2020 IEEE Symposium on Computers and communications (ISCC)*. IEEE, 2020.
- [45] S. Mirjalili., "Genetic algorithm." *Evolutionary algorithms and neural networks*. Springer, Cham, 2019. 43-55.